

Herschel/HIFI Observations of Molecular Lines Toward G10.47+0.03

Indrajit Mondal ¹, Prasanta Gorai ^{2,3,1*}, Ankan Das ¹, Suman Kumar Mondal ¹,
 Rubén Fedriani ⁴, Xiaohu Li ⁵, Parama Mahapatra ^{1,6}, Sabyasachi Banik ^{1,7},
 Sheng-Li Qin ⁸

¹ Institute of Astronomy Space and Earth Sciences, P 177, CIT Road, Scheme 7m, Kolkata 700054, West Bengal, India

² Rosseland Centre for Solar Physics, University of Oslo, PO Box 1029 Blindern, 0315, Oslo, Norway

³ Institute of Theoretical Astrophysics, University of Oslo, PO Box 1029 Blindern, 0315, Oslo, Norway

⁴ Instituto de Astrofísica de Andalucía, CSIC, Glorieta de la Astronomía s/n, 18008 Granada, Spain

⁵ Xinjiang Astronomical Observatory, Chinese Academy of Sciences, 150 Kexueyi St, Xinshi District, Ürümqi, Xinjiang 830011, China ⁶ Adamas University, Barbaria, Jagannathpur, District-24 Parganas (North), Kolkata 700126, West Bengal, India ⁷ St. Xavier's College (Autonomous), 30, Mother Teresa Sarani, Kolkata 700016, West Bengal, India

⁸ School of Physics and Astronomy, Yunnan University, Kunming 650106, China

Correspondence*:

Prasanta Gorai

prasanta.gorai@astro.uio.no

ABSTRACT

We present a spectral line analysis of the hot molecular core G10.47+0.03 (hereafter, G10). Our aim is to determine molecular abundances and excitation conditions across a wide spectral range inaccessible to ground-based observatories. We utilize archival data from the Herschel Space Observatory, obtained with the Heterodyne Instrument for the Far-Infrared (HIFI). We report here the detection of high-excitation CO, ¹³CO, and C¹⁸O, H₂O isotopologues, HCO⁺, HCN, HNC, CS, C³⁴S, SO, SO₂, H₂CS, and CH₃OH. CO, p-H₂O, CS, and HCN show similar velocity profiles with a narrow, blueshifted component, which may be linked to the outer outflow layer. Redshifted wings may indicate inner outflow activity. A Markov Chain Monte Carlo framework is employed to infer column densities and temperatures accurately. We also performed spectral energy distribution fitting to constrain the global physical parameters of G10, providing essential context for interpreting the molecular emission. The MCMC analysis revealed two excitation temperature components: a warm component (~30-65 K) and a hot component (~90-250 K). The higher temperatures indicate dense, hot gas typical of massive hot cores. The lower temperatures correspond to the warm, less dense envelope around the core. Transitions of H₂O, high-excitation CO, and HCN indicate outflowing gas and high-density shocked regions. These findings highlight G10's complex dynamical environment.

Keywords: astrochemistry, interstellar medium (ISM), Herschel/HIFI, molecular clouds, hot molecular core, star formation

1 INTRODUCTION

So far, about 340 molecular species have been detected in the interstellar medium (ISM) and circumstellar envelopes. Many of these species are complex and may play a role in the chemistry that could lead to the

emergence of life (see CDMS database¹, McGuire, 2022). Observations from ground-based telescopes have significantly advanced our understanding of molecular clouds and star-forming regions, enabling the discovery of new molecules and the mapping of their spatial distributions. However, a complete characterization of the chemical inventory in individual sources remains limited due to the lack of continuous, wide-frequency spectral line surveys. A large portion of this wide frequency is inaccessible from the ground due to atmospheric absorption. Comprehensive spectral line surveys are essential for advancing our understanding of chemical complexity in the ISM, the processes driving star and planet formation, and the gas-phase/ice-phase pathways leading to prebiotic chemistry (Garrod, 2013; Das, 2024; Ligterink et al., 2025). Such surveys provide access to a wide range of molecular and atomic transitions, enabling the determination of abundances, excitation conditions, and underlying physical parameters in diverse astrophysical environments. The development of high-resolution spectrometers, particularly aboard space-based observatories, have been instrumental in achieving these goals by extending spectral coverage beyond the limitations imposed by Earth's atmosphere (Zernickel et al., 2012; Kama et al., 2013; Kazmierczak et al., 2014).

The compact (<0.1 pc), hot (≥ 100 K), and dense ($\geq 10^6$ molecules per cubic centimeter) regions known as hot molecular cores (HMC) are exciting because they act as natural laboratories for the formation and evolution of complex organic molecules (COMs) (van Dishoeck and Blake, 1998; Mondal et al., 2023). HMCs are chemically rich gas-phase and grain-surface chemistry conditions, allowing the formation of COMs (Belloche et al., 2019; Jørgensen et al., 2020). These regions usually have a “forest” of molecular lines, suggesting a wide range of chemical species, from basic molecules like water (H_2O) and methanol (CH_3OH) to more complex prebiotic compounds like Propyl Cyanide ($\text{C}_3\text{H}_7\text{CN}$) (Belloche et al., 2009) and ethanolamine ($\text{NH}_2\text{CH}_2\text{CH}_2\text{OH}$) (Rivilla et al., 2021). G10.47+0.03 (hereafter, G10) is one of the notable hot cores located at a distance of 10.7 kpc from Earth (Urquhart et al., 2018). With a bolometric luminosity of approximately $7 \times 10^5 L_\odot$ (Cesaroni et al., 2010), G10 ranks among the most luminous hot cores in the Galaxy. This source has been observed with various ground-based facilities, including ALMA, SMA, and the VLA, and the results have been reported (Rolffs et al., 2011; Gorai et al., 2020a; Mondal et al., 2021, 2023).

The Herschel satellite was the first telescope designed for systematic investigation of the 500-5000 GHz (60-600 μm) frequency range (Pilbratt et al., 2010), while the Heterodyne Instrument for the Far Infrared (hereafter HIFI) was the first high-resolution spectrometer that allowed a comprehensive study of the 480-1907 GHz spectrum using heterodyne methods (de Graauw et al., 2010). The Herschel Key Project on EXtra-Ordinary Sources (HEXOS; (Bergin et al., 2010)) was developed to investigate the chemical composition of massive star-forming regions (Ceccarelli et al., 2010; De Luca et al., 2012; van der Tak et al., 2013a). In this project, Crockett et al. (2014), Tahani et al. (2016), and Nagy et al. (2017) conducted spectral line surveys at high frequencies, which are challenging to obtain through ground-based observations. They focused on Orion-KL, Orion South (referred to as Orion-S), and the Orion Bar, all of which are located in the Orion A Molecular Cloud, approximately 420 parsecs away (Menten et al., 2007). The HEXOS spectral surveys of Orion KL and Sgr B2 provide essential benchmarks for line identification, excitation analysis, and chemical complexity in massive star-forming regions. The line assignments and excitation conditions derived for G10 are therefore crucial for placing this source in context with these well-studied regions. However, Sgr B2 lies in the Central Molecular Zone, whereas G10 is a Galactic-disk hot molecular core with distinct physical conditions, kinematics, and evolutionary state. G10 hosts ultracompact H II regions and deeply embedded massive protostars, placing it at a different evolutionary stage from Orion

¹ <https://cdms.astro.uni-koeln.de/classic/molecules>

KL. Therefore, G10 cannot be treated as a simple scaled analogue of either CMZ sources such as Sgr B2 or nearby protoclusters like Orion KL. Earlier submillimeter observations (Mondal et al., 2023, 2021; Gorai et al., 2020b) revealed several COMs in G10. A high-frequency survey of G10 is thus essential to characterize the chemical and physical properties of this source across the submillimeter to far-infrared regime.

In this study, we present an in-depth analysis of the HIFI spectrum survey, focusing on G10 at high frequencies that are typically inaccessible to ground-based telescopes due to atmospheric absorption. The instrument detected a wide range of molecular lines, enabling a more in-depth understanding of G10's chemical complexity and physical conditions. This large data set is crucial for expanding our knowledge of star formation and the role of complex compounds in these processes.

2 METHODOLOGY

2.1 Observations

G10 has been observed with the HIFI, one of the three instruments of the Herschel Space Observatory (Pilbratt et al., 2010). The data reported in this work were taken from the Herschel Science Archive² (ID: OT_1pschilke_2, PI: P. Schilke, Dated: 12-10-2012). A summary of the observations is given in Table 1. The observations were performed covering five spectral ranges: (i) 514.7735-547.0775 GHz, (ii) 969.884-1001.195 GHz, (iii) 1020.363-1039.89 GHz, (iv) 1146.837-1181.16 GHz, and (v) 1205.8395-1226.5315 GHz. Each receiver band has separate channels for horizontal and vertical polarizations, equipped with a dedicated wide-band spectrometer with a native spectral resolution of 1.1 MHz (Roelfsema et al., 2012). The systematic velocity of this source has taken as 67 km s^{-1} (Rolffs et al., 2011; Gorai et al., 2020a; Mondal et al., 2023). All observations were conducted in Dual Beam Switch mode using the Fast Chop option, with a chopping frequency greater than 0.5 Hz. The noise of 1σ rms (0.035 K) is determined from the line-free regions of the spectrum adjacent to the lines. We obtained different RA and Dec for each observation, which are slightly shifted from the others. Across 515-1230 GHz, the expected FWHM is $40\text{-}18''$, whereas the pointing errors of $\leq 1\text{--}2''$ are therefore a small fraction (2–5% or less) of the beam.

Table 1. Details of the HERSCHEL/HIFI spectral survey towards the region G10.

Observation Id	RA (in J2000)	Dec (in J2000)	Band	Frequency Range (GHz)
1342242817	$18^h 08^m 38.19^s$	$-19^{\circ} 51' 49.55''$	1a	514.7735- 547.0775
1342244050	$18^h 08^m 38.22^s$	$-19^{\circ} 51' 50.23''$	4a	969.884-1001.195
1342244051	$18^h 08^m 38.22^s$	$-19^{\circ} 51' 50.18''$	4a	1020.363- 1039.89
1342253155	$18^h 08^m 38.27^s$	$-19^{\circ} 51' 49.32''$	5a	1146.837- 1181.16
1342253156	$18^h 08^m 38.26^s$	$-19^{\circ} 51' 49.41''$	5a	1205.8395-1226.5315

2.2 Line identification

Line identification is carried out using the CASSIS spectrum analyzer³. We consider unblended lines with a signal-to-noise ratio greater than the 3σ limit. Line parameters were obtained using a single Gaussian fit to the observed spectral profile of each unblended transition. The process involved using the Jet Propulsion

² <https://archives.esac.esa.int/hsa/whsa/>

³ <http://cassis.irap.omp.eu> (Vastel et al., 2015)

Laboratory (JPL, Pickett et al., 1998)⁴ and the Cologne Database for Molecular Spectroscopy (CDMS, Müller et al., 2001, 2005)⁵ spectral line databases to identify molecular species in our observed spectra. First, we identified the lines by visually evaluating each spectral characteristic in the HIFI bands and compared their transition frequencies to those specified in databases. We examined line blending, systematic velocity (VLSR), upper state energy (E_u), and the Einstein coefficient (A_{ij}) to confirm the identification of a molecular transition that corresponded to the spectra. Finally, we used local thermodynamic equilibrium (LTE) modeling to confirm or reject the assigned molecular species for the observed spectral feature.

We further evaluated all these transitions with non-LTE RADEX calculations (van der Tak et al., 2007) to determine their optical depth. For transitions found to be optically thin, we then employ Markov Chain Monte Carlo (MCMC) techniques within a local thermodynamic equilibrium (LTE) framework to generate synthetic spectra, enabling a quantitative assessment and validation of our molecular line identifications.

2.3 SED fitting

To complement the molecular line analysis, we performed a spectral energy distribution (SED) fitting for G10. This approach provides estimates of key physical parameters such as dust temperature, luminosity, and envelope mass, which cannot be directly obtained from line spectroscopy alone. These global properties serve as critical boundary conditions for interpreting the chemical complexity revealed by the HIFI survey. The spectral energy distribution (SED) analysis for our sample was carried out with the latest release (v0.9.11) of `sedcreator`, an open-source Python package detailed in Fedriani et al. (2023) and further discussed in Telkamp et al. (2025). The package is available on both GitHub⁶ and PyPi⁷, with full documentation at <https://sedcreator.readthedocs.io/>. `sedcreator` provides two primary classes: `SedFluxer`, which performs aperture photometry on specified images, coordinates, and aperture sizes using functions from Bradley et al. (2020); and `SedFitter`, which fits observations to a grid of models based on the radiative transfer framework of Zhang and Tan (2018).

3 RESULTS AND DISCUSSIONS

3.1 Physical properties of G10

The physical properties of the source G10 have been investigated in various works. The column density of the source, based on recent ALMA observations, has been reported to be $1.35 \times 10^{25} \text{ cm}^{-2}$, and the excitation temperature is around 150–400 K (Gorai et al., 2020a; Mondal et al., 2021, 2023). van der Tak et al. (2013a) reported a modeled envelope mass of 1168 M_\odot and a luminosity of $7 \times 10^5 \text{ L}_\odot$, based on an envelope size of 60000 AU and a source distance of 5.8 kpc. For SED fitting, we used archival data from Spitzer/IRAC (Werner et al., 2004; Fazio et al., 2004) at 3.6, 4.5, 5.8, and $8.0 \mu\text{m}$ from the Spitzer Heritage Archive, as well as Herschel/PACS and SPIRE Griffin et al. (2010) at 70, 160, 250, 350, and $500 \mu\text{m}$ from the ESA Herschel Science Archive. We also included MIPS 24 μm data. Herschel 70 μm data were used to automatically determine the optimal aperture using specialised functions from `sedcreator` (Fedriani et al., 2023), which was found to be 18 arcsec. This aperture was then applied as a fixed aperture to derive the fluxes from images at different wavelengths. In addition, we used an annulus of inner radius equal to the aperture radius and outer radius equal to $2 \times$ aperture radius to subtract the background from the fluxes.

⁴ (<http://spec.jpl.nasa.gov/>)

⁵ (<https://www.astro.uni-koeln.de/cdms>)

⁶ <https://github.com/fedriani/sedcreator>

⁷ <https://pypi.org/project/sedcreator/>

Figure 1 shows the SED fitting, while Figure 2 displays the 2D model fitting parameters of the source. The best-fit SED results are summarized in Table 2. Model parameters and derived quantities such as χ^2 is the chi-squared goodness-of-fit statistic, M_c is the core mass, Σ_{cl} is the mass surface density of the surrounding clump, R_c is the core radius, m_* is the current stellar mass, θ_{view} is the viewing angle measured from the outflow axis, A_V is the visual extinction along the line of sight, M_{env} is the envelope mass, $\theta_{\text{w,esc}}$ is the half-opening angle of the outflow cavity (escape angle), \dot{M}_{disk} is the disk mass accretion rate onto the star, $L_{\text{bol,iso}}$ is the isotropic bolometric luminosity, and L_{bol} is the true bolometric luminosity of the source. Our SED-derived luminosity is comparable to the previously reported value (van der Tak et al., 2013b). From the mass surface density (Σ_{cl}), we can estimate the molecular hydrogen column density (N_{H_2}) using the following relation:

$$N_{\text{H}_2} = \frac{\Sigma_{\text{cl}}}{\mu m_{\text{H}}}.$$

Here, m_{H} is the hydrogen atomic mass and $\mu = 2.8$ is the mean molecular weight per H_2 molecule (including helium). The value of Σ_{cl} obtained from our best fitted model is 3.16, yields $N_{\text{H}_2} = 6.74 \times 10^{23} \text{ cm}^{-2}$. This value is slightly lower than that reported in previous ALMA observations. This difference arises from the larger spatial coverage achieved using the optimal aperture method, which encompasses an extended envelope in our analysis. This extended envelope is also probed by Herschel observations, whereas earlier column density measurements were based on high-resolution ALMA observations and focused on the compact, dense core.

Table 2. Best fitted SED parameters.

χ^2	M_c (M_{\odot})	Σ_{cl} (g cm^{-2})	R_c (pc)	m_* (M_{\odot})	θ_{view} (deg)	A_V (mag)	M_{env} (M_{\odot})	$\theta_{\text{w,esc}}$ (deg)	\dot{M}_{disk} ($M_{\odot} \text{ yr}^{-1}$)	$L_{\text{bol,iso}}$ (L_{\odot})	L_{bol} (L_{\odot})
6.76	480.00	3.16	0.09	24.00	82.82	56.13	440.54	11.50	1.95e-03	2.43e+05	2.94e+05
8.21	480.00	1.00	0.16	32.00	22.33	160.02	414.30	18.51	9.31e-04	3.72e+05	2.95e+05
7.23	400.00	3.16	0.08	24.00	85.70	67.09	361.65	12.84	1.86e-03	2.34e+05	3.01e+05
10.08	400.00	1.00	0.15	32.00	22.33	218.17	329.80	20.63	8.74e-04	7.17e+05	2.85e+05
10.09	480.00	1.00	0.16	64.00	12.84	333.10	324.63	31.74	1.21e-03	4.75e+06	8.41e+05

Note- The best five models taken from the 432 physical models for the non-restricted Σ_{cl} case. χ^2 is the chi-squared goodness-of-fit statistic, M_c is the core mass, Σ_{cl} is the mass surface density of the surrounding clump, R_c is the core radius, m_* is the current stellar mass, θ_{view} is the viewing angle measured from the outflow axis, A_V is the visual extinction along the line of sight, M_{env} is the envelope mass, $\theta_{\text{w,esc}}$ is the half-opening angle of the outflow cavity (escape angle), \dot{M}_{disk} is the disk mass accretion rate onto the star, $L_{\text{bol,iso}}$ is the isotropic bolometric luminosity, and L_{bol} is the true bolometric luminosity of the source.

3.2 Identified species

Here, we present the results of the molecular line survey conducted with HIFI toward the hot molecular core G10. The broad spectral coverage of HIFI enables a comprehensive investigation of molecular emission, ranging from simple diatomic species to complex organic molecules, thereby highlighting the remarkable chemical diversity of this source. The species identified in this survey are listed in Table 3 and shown in Figure 3, which reflects the rich inventory characteristic of hot cores.

To provide quantitative constraints, all detected transitions are catalogued in Table 4, including their rest frequencies, upper-state energies (E_u), line widths (FWHM), peak intensities, and integrated intensities ($\int T_{\text{mb}} dv$), where T_{mb} is the main beam temperature obtained from the observations in Kelvin and v is the FWHM in km s^{-1} . This compilation serves as the basis for subsequent analyses, including rotational

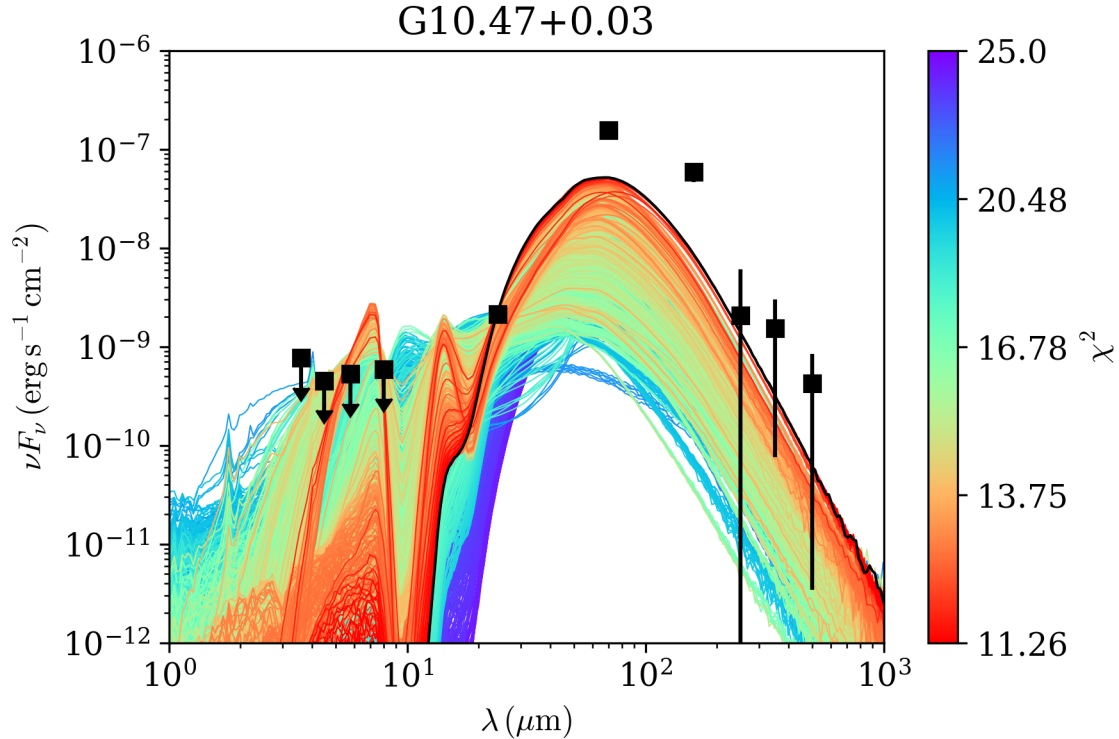


Figure 1. SED fitting of G10. The fixed-aperture, background-subtracted SED data were fitted using the (Zhang and Tan, 2018) protostellar model grid, and the best-fitting model is shown as a black line while all other “good” model fits (see text) are shown with colored lines (red to blue with increasing χ^2). We define good models as those with χ^2 values up to twice the minimum χ^2 value, i.e., $\chi^2 < 2 \chi^2_{\min}$ (Fedriani et al., 2023; Telkamp et al., 2025).

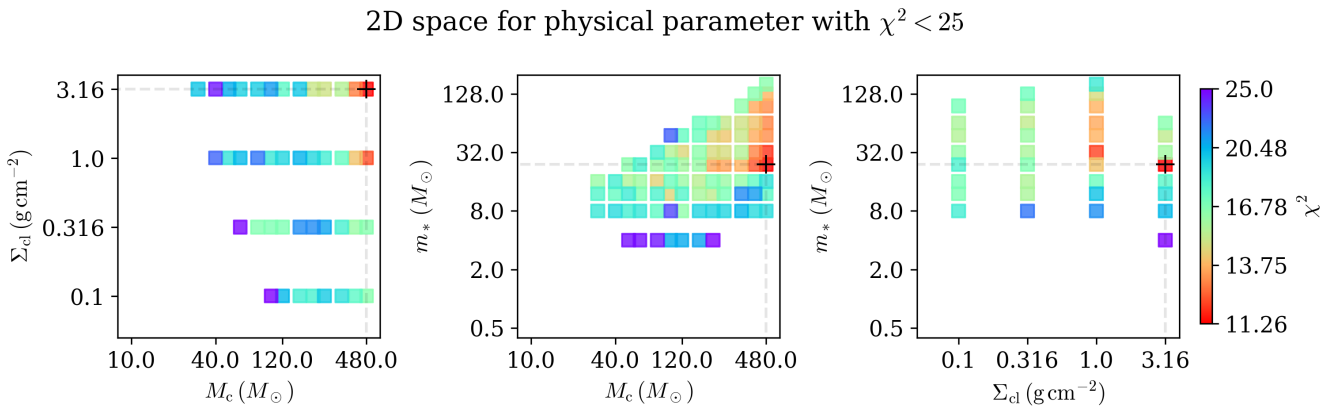


Figure 2. Comparison of key model parameters for each source: Σ_{cl} vs. M_c (left column), m_* vs. M_c (center column), and m_* vs. Σ_{cl} (right column). Only the “good” model fits are shown, color-coded by their χ^2 values. The black cross marks the best-fitting model.

diagram modeling and LTE radiative transfer calculations, aimed at deriving column densities and excitation conditions for the identified species.

The observed molecules serve as key tracers of various physical properties of the present source. CO and its isotopologues trace large-scale gas and outflows, while species such as HCN, H₂O, HCO⁺, CS, and SO

Table 3. List of species identified in G10 from this survey.

Diatomeric Molecules	Multi-atomic Molecules	Ionized
CO	HCN, v=0	HCO ⁺ , v=0,1,2
¹³ CO	H ₂ ¹⁸ O	OH ⁺ ^b
C ¹⁸ O	o-H ₂ O	HC ¹⁸ O ⁺ ^a
CS	p-H ₂ O	...
C ³⁴ S	H ₂ CS	...
SO	CH ₃ OH, vt=0-2	...
N ¹⁷ O ^a
NH ^b	NH ₂	...
...	SO ₂	...
...	HNC	...
...	CH ₃ OCH ₃ , v=0 ^a	...
...	H ₂ ¹⁷ O	...
...	H ₂ S ^b
...	D ₂ CO ^a	...
...	HC(O)NH ₂ , v=0 ^a	...
...	NH ₃ ^b	...
...	³³ SO ₂ ^a	...
...	³⁴ SO ₂ ^a	...
...	SO ¹⁷ O ^a	...
...	HCO ^a	...

^a Below three sigma or blended with other transitions, ^b Observed absorption profiles.

probe dense and warm regions associated with infall and shock activity. The detection of complex organic molecules such as CH₃OH and H₂CS indicates the presence of high-temperature, high-density gas, typical of hot molecular cores.

3.2.1 Column density estimation

Rotational diagram analysis

This analysis assumes that the detected transitions are optically thin in LTE. For optically thin lines, the column density can be calculated using the expression (Goldsmith and Langer, 1999) as

$$\frac{N_u^{thin}}{g_u} = \frac{3k_B \int T_{mb} dv}{8\pi^3 \nu S \mu^2}, \quad (1)$$

where g_u is the degeneracy of the upper state, k_B is the Boltzmann constant, $\int T_{mb} dv$ is the integrated intensity, ν is the rest frequency, μ is the electric dipole moment, and S is the transition line strength.

The total column densities N_{total} under LTE conditions can be written as,

$$\frac{N_u^{thin}}{g_u} = \frac{N_{total}}{Q(T_{rot})} e^{(-E_u/k_B T_{rot})}, \quad (2)$$

where E_u is the upper-state energy and $Q(T_{rot})$ is the partition function at rotational temperature T_{rot} . Using the logarithm of both sides of the above equation 2, it gives

$$\log \left(\frac{N_u^{thin}}{g_u} \right) = - \left(\frac{\log e}{T_{rot}} \right) \left(\frac{E_u}{k_B} \right) + \log \left(\frac{N_{total}}{Q(T_{rot})} \right). \quad (3)$$

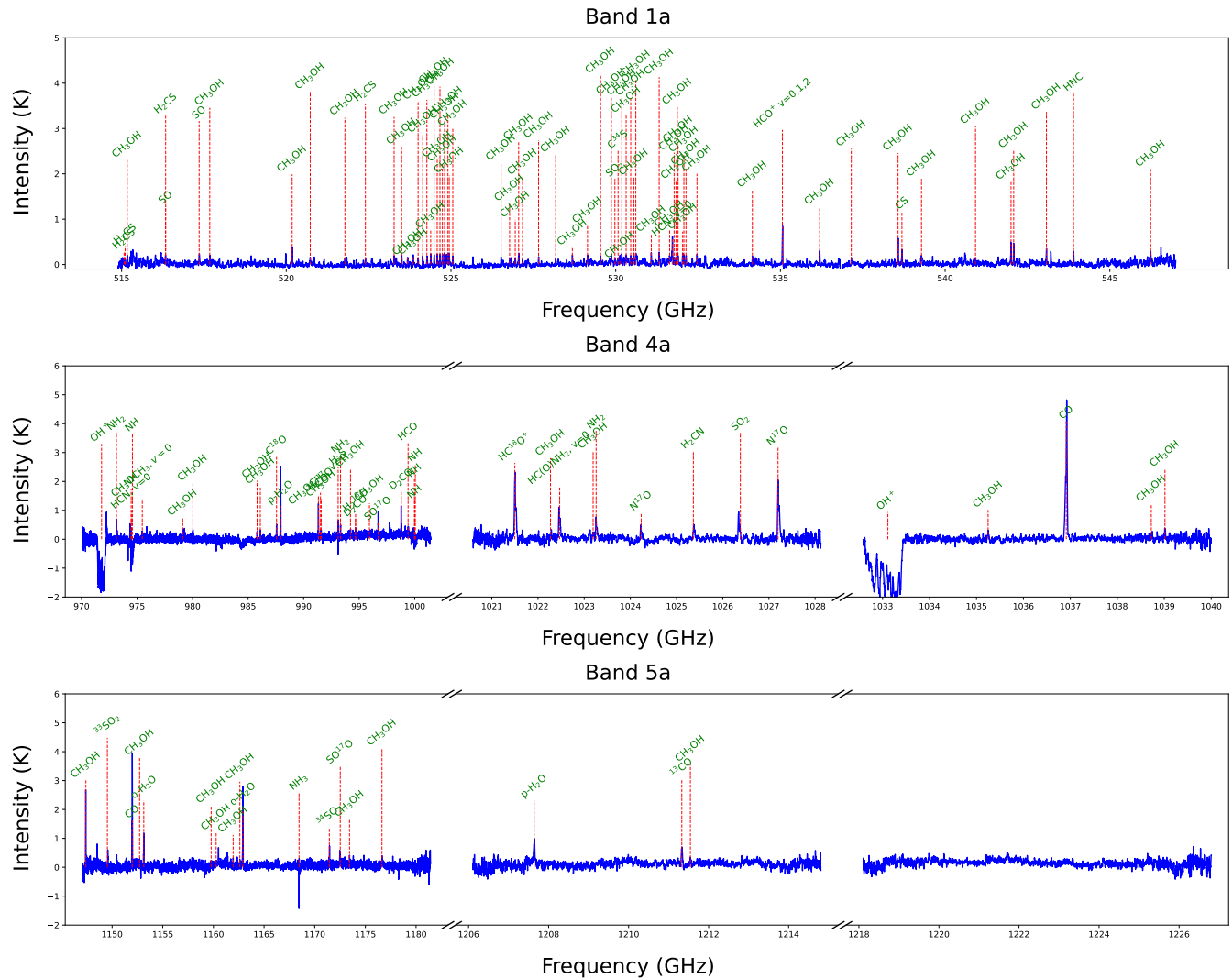


Figure 3. G10 Spectra with identified species.

This expresses a linear relationship in logarithmic space between the upper-state energy and the column density of the corresponding level, allowing both the excitation temperature and total column density of a species to be derived simultaneously through rotational diagram analysis.

Among the detected species, methanol (CH_3OH , $vt=0-2$) and thioformaldehyde (H_2CS) exhibit multiple transitions. However, in the case of H_2CS , four transitions were identified, two of which show significantly narrower line widths compared to the others, making a consistent rotational analysis unreliable. We therefore restrict our rotational diagram analysis to methanol, from which excitation temperatures and column densities were derived (see Figure 4).

Table 4 Summary of the Line Parameters of Observed Molecules toward G10.

Species	Quantum number	Frequency (GHz)	E_u (K)	FWHM (km s $^{-1}$)	Peak intensity (K)	$\int T_{mb} dv$ (K km s $^{-1}$)
CH ₃ OH,	(2 _{2,0,2} - 1 _{1,1,2}) (12 _{4,9,2} - 12 _{3,9,2})	520.179054* 524.384667	32.86 268.91	7.69 \pm 0.29 9.08 \pm 0.23	0.378 \pm 0.006 0.234 \pm 0.003	3.099 \pm 0.173 2.264 \pm 0.088

Continued on next page

Table 4 continued from previous page

Species	Quantum number	Frequency (GHz)	E_u (K)	FWHM (km s ⁻¹)	Peak intensity (K)	$\int T_{mb} dv$ (K km s ⁻¹)
vt=0-2	(11 _{4,8,2} – 11 _{3,8,2})	524.488918	241.07	5.76 ± 0.16	0.220 ± 0.003	1.348 ± 0.054
	(10 _{4,7,2} – 10 _{3,7,2})	524.582604	215.55	9.55 ± 0.34	0.235 ± 0.003	2.388 ± 0.123
	(9 _{4,6,2} – 9 _{3,6,2})	524.666219	192.34	8.63 ± 0.40	0.232 ± 0.004	2.134 ± 0.135
	(7 _{4,4,2} – 7 _{3,4,2})	524.804977	152.89	8.57 ± 0.41	0.258 ± 0.003	2.353 ± 0.148
	(14 _{2,13,0} – 14 _{1,14,0})	526.520131	281.29	5.80 ± 0.31	0.179 ± 0.004	1.108 ± 0.084
	(14 _{3,12,1} – 14 _{2,13,1})	527.658026	291.46	6.52 ± 0.51	0.173 ± 0.005	1.202 ± 0.133
	(11 _{3,9,1} – 11 _{2,10,1})	529.143188	200.92	10.48 ± 0.53	0.210 ± 0.004	2.339 ± 0.164
	(11 _{1,10,1} – 10 _{1,9,1})	532.031395*	174.26	9.15 ± 0.23	0.259 ± 0.003	2.525 ± 0.093
	(11 _{2,10,1} – 10 _{2,9,1})	532.466250*	175.53	8.29 ± 0.17	0.235 ± 0.002	2.070 ± 0.062
	(11 _{1,10,0} – 10 _{1,9,0})	536.191058*	169.01	10.31 ± 0.37	0.307 ± 0.004	3.365 ± 0.165
	(10 _{2,8,0} – 9 _{1,9,0})	986.097819	165.40	8.79 ± 0.65	0.300 ± 0.013	2.810 ± 0.341
	(8 _{3,6,1} – 8 _{2,7,1})	530.123296	131.28	7.49 ± 0.36	0.206 ± 0.004	1.645 ± 0.110
	(7 _{3,5,1} – 7 _{2,6,1})	530.316194	112.71	7.71 ± 0.32	0.218 ± 0.002	1.786 ± 0.092
	(6 _{3,4,1} – 6 _{2,5,1})	530.454670	96.46	12.72 ± 0.31	0.205 ± 0.002	2.769 ± 0.094
	(5 _{3,3,1} – 5 _{2,4,1})	530.549228	82.53	8.27 ± 0.17	0.252 ± 0.002	2.220 ± 0.062
	(4 _{3,2,1} – 4 _{2,3,1})	530.610267	70.93	7.31 ± 0.28	0.251 ± 0.003	1.956 ± 0.102
	(5 _{1,5,0} – 4 _{0,4,0})	538.570553*	49.06	8.43 ± 0.23	0.582 ± 0.005	5.218 ± 0.190
	(6 _{3,4,0} – 5 _{2,3,0})	542.000954*	98.55	9.37 ± 0.14	0.495 ± 0.002	4.938 ± 0.104
	(6 _{3,3,0} – 5 _{2,4,0})	542.081952*	98.55	7.21 ± 0.18	0.473 ± 0.004	3.634 ± 0.130
	(8 _{0,8,1} – 7 _{1,7,2})	543.076175*	96.61	9.24 ± 0.31	0.351 ± 0.004	3.455 ± 0.157
	(16 _{0,16,0} – 15 _{1,15,0})	515.170245	315.21	10.21 ± 0.29	0.209 ± 0.002	2.273 ± 0.093
	(19 _{7,12,2} – 20 _{6,14,2})	516.922004	700.76	4.99 ± 0.39	0.103 ± 0.005	0.546 ± 0.073
	(16 _{2,15,0} – 15 _{3,12,0})	517.676592	353.12	7.82 ± 0.28	0.213 ± 0.004	1.770 ± 0.105
	(13 _{5,9,0} – 14 _{4,10,0})	521.776019	349.05	10.50 ± 0.66	0.142 ± 0.003	1.592 ± 0.142
	(24 _{4,21,2} – 24 _{3,21,2})	522.046360	783.40	4.68 ± 0.32	0.094 ± 0.003	0.467 ± 0.048
	(19 _{4,16,2} – 19 _{3,16,2})	523.306240	528.59	8.05 ± 0.28	0.134 ± 0.002	1.144 ± 0.056
	(21 _{3,19,1} – 21 _{2,20,1})	529.038126	583.96	5.59 ± 0.41	0.136 ± 0.003	0.809 ± 0.079
	(11 _{8,4,2} – 10 _{8,3,2})	531.437209	474.56	7.23 ± 0.25	0.129 ± 0.002	0.994 ± 0.053
	(11 _{8,3,0} – 10 _{8,2,0})	531.460073	474.06	9.15 ± 0.35	0.137 ± 0.002	1.337 ± 0.072
	(6 _{2,5,5} – 7 _{3,5,5})	537.151571	413.23	6.55 ± 0.24	0.153 ± 0.003	1.068 ± 0.062
	(17 _{1,17,3} – 17 _{2,15,3})	545.755816	678.86	3.55 ± 0.09	0.217 ± 0.002	0.820 ± 0.028
	(14 _{4,11,2} – 14 _{3,11,2})	524.142239	331.53	8.95 ± 0.90	0.186 ± 0.005	1.771 ± 0.232
CO	(10 - 9)	1151.985452	304.16	7.98 ± 0.27	3.731 ± 0.085	31.68 ± 1.30
	(9 - 8)	1036.912393	248.88	6.31 ± 0.10	4.803 ± 0.054	32.27 ± 0.63
¹³ CO	(11 - 10)	1211.329661	348.92	9.31 ± 0.22	0.662 ± 0.011	6.56 ± 0.20
	(9 - 8)	991.329305	237.93	8.74 ± 0.07	1.246 ± 0.008	11.59 ± 0.12
C ¹⁸ O	(9 - 8)	987.56040	237.03	8.27 ± 0.26	0.485 ± 0.013	4.27 ± 0.19
CS	(11 - 10)	538.68883	155.15	11.70 ± 0.40	0.300 ± 0.006	3.73 ± 0.15
C ³⁴ S	(11 - 10)	530.071221	152.66	9.12 ± 1.73	0.158 ± 0.005	1.54 ± 0.30
SO	(12 _{1,3} – 11 _{1,2})	517.3543051	165.78	14.07 ± 0.32	0.236 ± 0.003	3.53 ± 0.11
	(12 _{1,2} – 11 _{1,1})	516.3354166	174.22	14.27 ± 0.39	0.185 ± 0.004	2.82 ± 0.09
SO ₂	(9 _{4,6} – 8 _{3,5})	529.97493	80.64	8.58 ± 0.40	0.147 ± 0.004	1.34 ± 0.07
³³ SO ₂	(23 _{4,20,24.5} – 22 _{1,21,23.5})	1149.533678	292.80	10.13 ± 0.49	0.460 ± 0.019	4.95 ± 0.32
³⁴ SO ₂	(26 _{2,24} – 25 _{1,25})	1171.444506	339.63	10.78 ± 0.24	0.701 ± 0.012	8.04 ± 0.22
SO ¹⁷ O	(29 _{5,24} – 28 _{4,25})	996.700636	450.31	8.28 ± 0.24	0.829 ± 0.018	7.30 ± 0.27

Continued on next page

Table 4 continued from previous page

Species	Quantum number	Frequency (GHz)	E_u (K)	FWHM (km s $^{-1}$)	Peak intensity (K)	$\int T_{mb} dv$ (K km s $^{-1}$)	
	(25 _{3,23} – 24 _{0,24})	1172.520701	312.02	14.52 ± 0.41	0.533 ± 0.009	8.24 ± 0.27	
o-H ₂ O	(3 _{1,2} – 2 _{2,1})	1153.126822	215.20	11.82 ± 0.36	1.099 ± 0.025	13.83 ± 0.53	
	(3 _{2,1} – 3 _{1,2})	1162.911593	271.01	10.26 ± 0.26	2.572 ± 0.050	28.09 ± 0.89	
p-H ₂ O	(2 _{0,2} – 1 _{1,1})	987.926764	100.85	12.29 ± 0.44	1.950 ± 0.057	25.52 ± 1.18	
	(4 _{2,2} – 4 _{1,3})	1207.638714	454.34	9.76 ± 0.33	0.941 ± 0.018	9.77 ± 0.38	
H ₂ ¹⁸ O	2 _{0,2} – 1 _{1,1}	994.675129	100.61	11.75 ± 0.37	0.385 ± 0.058	4.82 ± 0.74	
H ₂ ¹⁷ O	(2 _{0,2} – 1 _{1,1})	991.52013	100.72	10.07 ± 0.51	0.269 ± 0.007	2.88 ± 0.16	
HCN, v=0	(6 - 5)	531.7163479	89.32	10.65 ± 0.84	0.526 ± 0.025	5.97 ± 0.55	
	(11 - 10)	974.4871998	280.67	2.88 ± 0.14	0.400 ± 0.017	1.23 ± 0.08	
HNC	(6 - 5)	543.897386	91.37	5.42 ± 0.10	0.288 ± 0.004	1.66 ± 0.04	
OH ⁺	(1 _{2,1,5} – 0 _{1,0,5})	971.8053	46.64	
	(1 _{1,0,5} – 0 _{1,1,5})	1033.1129	49.58	
NH	(1 _{2,2,5,2,5} – 0 _{1,1,5,1,5})	974.4708	46.77	
	(1 _{1,1,5,1,5} – 0 _{1,1,5,2,5})	1000.00102	47.99	
NH ₂	(2 _{2,0,0,7,2,5} – 2 _{1,1,0,14,1,5})	993.3229713	167.87	10.19 ± 0.21	0.473 ± 0.006	5.13 ± 0.14	
NH ₃	(2 _{1,0} – 1 _{1,1})	1168.452394	79.34	
N ¹⁷ O	(10 _{-1,10,5,10} – 9 _{1,9,5,10})	1024.234273	280.93	9.95 ± 0.72	0.374 ± 0.021	3.97 ± 0.37	
	(10 _{-1,10,5,12} – 9 _{-1,9,5,11})	1027.197994	280.92	13.66 ± 1.22	1.526 ± 0.078	22.20 ± 2.28	
H ₂ S	(3 _{0,3} – 2 _{1,2})	993.108247	102.76	
H ₂ CS	(15 _{3,13} – 14 _{3,12})	515.075721	316.22	4.32 ± 0.11	0.148 ± 0.001	0.68 ± 0.05	
	(15 _{3,12} – 14 _{3,11})	515.10836	316.22	7.92 ± 0.99	0.116 ± 0.002	0.98 ± 0.14	
	(15 _{2,13} – 14 _{2,12})	516.337197	250.71	13.43 ± 1.51	0.192 ± 0.004	2.74 ± 0.32	
	(15 _{1,14} – 14 _{1,13})	522.40314	213.87	9.93 ± 0.48	0.122 ± 0.003	1.29 ± 0.07	
HCO ⁺ v=0,1,2	(6 _{0,0} – 5 _{0,0})	535.061402	89.88	9.36 ± 0.20	0.831 ± 0.014	8.27 ± 0.22	
HC ¹⁸ O ⁺	(12 - 11)	1021.498294	318.72	7.40 ± 0.11	2.285 ± 0.023	17.99 ± 0.32	
HCO	(10 _{2,9,10,5,10} 11 _{1,10,11,5,11})	–	999.402896	359.86	12.74 ± 0.58	0.409 ± 0.008	5.54 ± 0.28
D ₂ CO	(17 _{3,15} – 16 _{3,14})	994.673348	479.38	13.38 ± 0.28	0.340 ± 0.004	4.84 ± 0.13	
	(17 _{6,11} – 16 _{6,10})	998.7898855	624.30	9.03 ± 0.41	0.872 ± 0.026	8.38 ± 0.45	
CH ₃ OCH ₃ , v=0	(16 _{12,4,3} – 15 _{11,4,3})	975.469645	325.97	7.10 ± 0.35	0.243 ± 0.008	1.84 ± 0.12	
	(23 _{10,13,1} – 22 _{9,13,1})	991.343273	391.66	8.72 ± 0.08	1.246 ± 0.008	11.56 ± 0.13	
HC(O)NH ₂ , v=0	(22 _{5,17} – 21 _{4,18})	1022.469579	332.60	14.58 ± 1.19	0.881 ± 0.036	13.68 ± 1.25	

* Optically thick transition.

Markov Chain Monte Carlo (MCMC) method

To analyze the line profiles of the observed species toward the hot core G10, we employ the MCMC approach under the assumption of LTE. We have extracted the best-fitted key physical parameters, including the column density, excitation temperature, line width (FWHM), optical depth, and systemic velocity (V_{LSR}). We used the Python scripting interface of CASSIS to derive the best-fitting physical parameters of the source through a χ^2 minimization between the modeled and

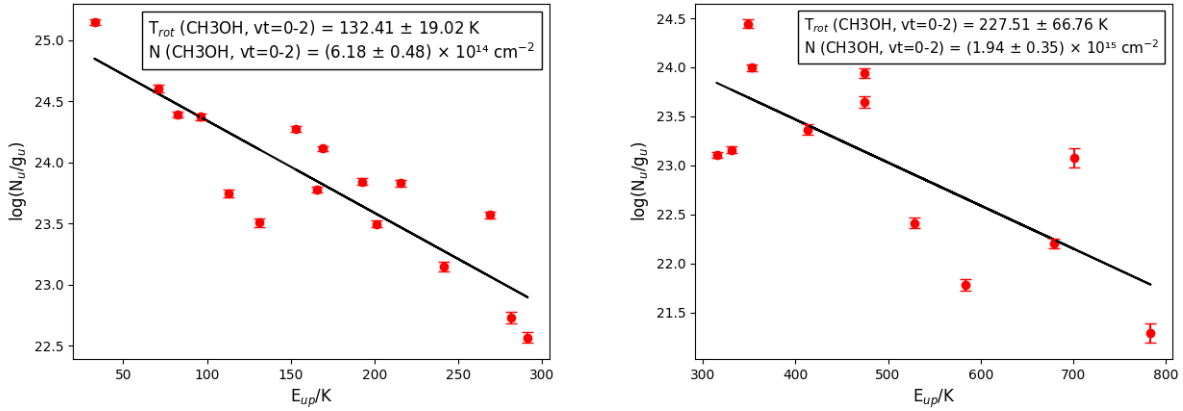


Figure 4. Above two diagrams present the rotational spectrum for transitions occurring below and above 300 K for CH_3OH ($vt=0-2$). The vertical bars indicate the error margins for the measurements in each panel. Each panel provides the best-fitted values for the rotational temperature and column density.

observed spectra across N transitions. The χ^2 value was computed as

$$\chi_i^2 = \sum_{j=1}^{N_i} \frac{(I_{ij}^{\text{obs}} - I_{ij}^{\text{model}})^2}{(\text{rms}_i^2 + (I_{ij}^{\text{obs}} \times \text{cal}_i)^2)}, \quad (4)$$

where I_{ij}^{obs} and I_{ij}^{model} are the observed and modeled intensities for channel j of transition i , rms_i is the spectral noise, and cal_i is the calibration uncertainty. The reduced χ^2 was obtained as

$$\chi_{\text{red}}^2 = \frac{1}{\sum_i^{N_{\text{spec}}} N_i} \sum_{i=1}^{N_{\text{spec}}} \chi_i^2. \quad (5)$$

In the MCMC computation, initial parameter values were randomly selected within the user-defined range $[X_{\text{min}}, X_{\text{max}}]$. The step at iteration l was defined as

$$\theta_{l+1} = \theta_l + \alpha(v - 0.05), \quad (6)$$

where v is a random number between 0 and 1. The step amplitude α is expressed as $\alpha = \frac{k(X_{\text{max}} - X_{\text{min}})}{k'}$, with

$$k = \begin{cases} r_c, & l > c, \\ \frac{(r_c - 1)}{c}l + 1, & l < c, \end{cases}$$

where c and r_c are the cutoff and cutoff ratio, respectively, while k' is a reduced physical parameter. This approach ensures larger steps at the beginning for efficient parameter exploration and smaller steps near convergence to accurately determine the optimal χ^2 .

The line parameters obtained with these calculations are summarized in Table 5. The corresponding observed spectra, overlaid with the best-fit LTE models, are presented in Figures 5, 6, and 7.

METHANOL (CH_3OH): It is one of the most abundant COMs in the ISM and plays a central role in the chemical evolution of star-forming regions. Our Herschel/HIFI spectral line investigation of the hot molecular core G10 revealed multiple transitions of methanol, spanning a wide range of upper-state energy levels from 32.86 K to 783.40 K (see Table 4). The rotational diagram of methanol shown in Figure 4 clearly indicates that better fitting results would be obtained if we consider two temperature components. Two panels of Figure 4 show that a more accurate estimate of the column density and rotational

Table 5. Summary of the best-fitted line parameters obtained by using the MCMC method.

Species	Frequency (GHz)	FWHM Range (km.s ⁻¹)	Best fit FWHM	Column Density (cm ⁻²)		T _{ex} (K)		Source Size (")	V _{LSR} (km.s ⁻¹)		Optical Depth (τ)		
				Range		Best fit			Range				
				Range	Best fit	Range	Best fit		Range	Best fit			
SO	517.3543	6–12	6.99 ± 0.45	1.0 × 10 ¹³ –1.0 × 10 ¹⁵	(3.60 ± 0.98) × 10 ¹⁴	20–100	45.72 ± 5.55	39.45 ± 0.77	66–68	66.97 ± 0.71	1.34 × 10 ⁻²		
	516.3354			1.0 × 10 ¹³ –1.0 × 10 ¹⁵	(2.90 ± 0.87) × 10 ¹⁴	20–100	31.66 ± 6.70		39.32 ± 0.26	66.5–67.5	67.44 ± 0.04		
SO ₂	529.9749	6–10	9.90 ± 0.08	1.0 × 10 ¹³ –1.0 × 10 ¹⁵	(2.90 ± 0.87) × 10 ¹⁴	20–100	31.66 ± 6.70	39.32 ± 0.26	66.5–67.5	67.44 ± 0.04	1.70 × 10 ⁻²		
CS	538.68883	4–7	5.1 ± 0.1	1.0 × 10 ¹² –2.0 × 10 ¹⁶	(7.85 ± 5.4) × 10 ¹³	20–60	31.0 ± 1.1	34.3 ± 0.4	64–67	65.1 ± 0.1	4.1 × 10 ⁻²		
				8–15	10.6 ± 0.2	1.0 × 10 ¹² –2.0 × 10 ¹⁶	(4.31 ± 1.29) × 10 ¹³		69–75	73.8 ± 0.1	1.0 × 10 ⁻²		
C ³⁴ S	530.0712	6–9	7.69 ± 0.91	1.0 × 10 ¹² –1.0 × 10 ¹⁴	(2.91 ± 0.52) × 10 ¹³	20–100	42.49 ± 2.13	39.59 ± 0.07	64–67	66.86 ± 0.18	1.06 × 10 ⁻²		
	994.675129			9.2 ± 0.6	5.0 × 10 ¹² –5.0 × 10 ¹⁶	(1.37 ± 0.5) × 10 ¹⁴	20–70	23.2 ± 2.1	29.2 ± 3.4	67–70	69.5 ± 0.1		
H ₂ ¹⁸ O	991.520129	3–8	6.6 ± 0.5	1.0 × 10 ¹² –1.0 × 10 ¹⁵	(8.4 ± 4.2) × 10 ¹³	20–70	29.4 ± 2.2	31.1 ± 1.3	64–69	66.5 ± 1.1	1.1 × 10 ⁻¹		
	1153.126822			1162.9116	6–8	7.59 ± 0.48	5.0 × 10 ¹⁴ –5.0 × 10 ¹⁶	(1.69 ± 0.43) × 10 ¹⁶	20–100	38.28 ± 1.42	18.12 ± 0.12		
p-H ₂ O	987.9268	4–7	4.5 ± 0.1	1.0 × 10 ¹¹ –2.0 × 10 ¹⁶	(6.33 ± 0.4) × 10 ¹³	20–60	30.0 ± 1.1	34.4 ± 0.4	62–65	63.5 ± 0.1	3.0 × 10 ⁻¹		
				5–15	11.02 ± 0.28	1.0 × 10 ¹¹ –8.0 × 10 ¹⁶	(4.81 ± 0.4) × 10 ¹³		80–150	97.25 ± 0.1	67–71	69.9 ± 0.1	
HCN	531.7164	4–7	5.06 ± 0.1	1.0 × 10 ¹² –2.0 × 10 ¹⁶	(1.10 ± 0.90) × 10 ¹⁴	20–60	23.9 ± 3.1	36.3 ± 1.0	60–66	63.5 ± 0.3	1.0 × 10 ⁻¹		
				5–15	11.9 ± 0.4	1.0 × 10 ¹² –5.0 × 10 ¹⁶	(1.72 ± 0.60) × 10 ¹³		80–150	94.9 ± 2.3	20.3 ± 0.6		
HNC	543.8974	4–7	5.30 ± 0.22	1.0 × 10 ¹² –1.0 × 10 ¹⁶	(2.86 ± 0.70) × 10 ¹³	10–100	21.74 ± 1.46	30.03 ± 1.14	62–67	63.9 ± 0.24	4.87 × 10 ⁻²		
	993.322971			7.1 ± 0.5	1.0 × 10 ¹³ –1.0 × 10 ¹⁵	(3.6 ± 0.6) × 10 ¹⁴	10–100	30.8 ± 0.7	34.1 ± 1.9	66–70	67.8 ± 0.9		
HCO ⁺	535.0614	4–8	6.81 ± 1.14	1.0 × 10 ¹² –1.0 × 10 ¹⁴	(3.75 ± 1.31) × 10 ¹³	10–100	23.29 ± 3.82	39.26 ± 0.14	64–66	65.34 ± 0.38	2.11 × 10 ⁻¹		
	991.3293			7–12	9.6 ± 0.1	3.0 × 10 ¹³ –8.0 × 10 ¹⁶	(1.8 ± 0.53) × 10 ¹⁶	10–130	64.5 ± 7.9	23.08 ± 3.28	66–69	66.7 ± 0.1	
C ¹⁸ O	987.564	5–10	7.59 ± 1.42	1.0 × 10 ¹³ –1.0 × 10 ¹⁸	(1.80 ± 0.85) × 10 ¹⁷	10–100	40.34 ± 9.16	18.67 ± 0.27	64–69	65.63 ± 0.94	1.67 × 10 ⁻¹		
	1211.3297										1.98 × 10 ⁻²		
CO	1036.9124	4–7	5.1 ± 0.3	1.0 × 10 ¹³ –2.0 × 10 ¹⁷	(5.5 ± 2.3) × 10 ¹⁶	20–60	41.3 ± 9.9	37.5 ± 2.0	62–65	63.3 ± 0.2	2.34 × 10 ⁻¹		
	1151.9855			5–12	11.0 ± 0.4	1.0 × 10 ¹³ –8.0 × 10 ¹⁷	(3.7 ± 0.6) × 10 ¹⁶		80–150	104.5 ± 6.5	20.0 ± 1.0		
H ₂ CS	516.3372	6–10	8.37 ± 1.20	1.0 × 10 ¹³ –1.0 × 10 ¹⁶	(1.65 ± 0.94) × 10 ¹⁵	20–100	54.52 ± 12.95	31.0 ± 4.71	65–67	66.38 ± 0.2	2.38 × 10 ⁻²		
	522.4031										2.61 × 10 ⁻²		
CH ₃ OH (v _l =0–2) (E _u < 300 K)	524.384667	4–12	6.17 ± 0.91	1.0 × 10 ¹³ –1.0 × 10 ¹⁵	(6.24 ± 3.31) × 10 ¹⁴	20–200	117.55 ± 23.58	28.42 ± 7.44	62–67	66.18 ± 0.81	2.62 × 10 ⁻³		
	524.488918										2.97 × 10 ⁻³		
	524.582604										3.27 × 10 ⁻³		
	524.666219										3.47 × 10 ⁻³		
	524.804977										3.42 × 10 ⁻³		
	526.520131										2.68 × 10 ⁻³		
	527.658026										3.16 × 10 ⁻³		
	529.143188										5.02 × 10 ⁻³		
	530.123296										6.13 × 10 ⁻³		
	530.316194										6.08 × 10 ⁻³		
CH ₃ OH (v _l =0–2) (E _u > 300 K)	530.454670	4–12	8.58 ± 0.47	1.0 × 10 ¹³ –1.0 × 10 ¹⁶	(2.80 ± 0.71) × 10 ¹⁵	20–400	240.78 ± 97.12	29.74 ± 5.14	62–67	66.50 ± 0.35	4.16 × 10 ⁻³		
	530.549228										1.32 × 10 ⁻⁴		
	530.610267										1.09 × 10 ⁻³		
	986.097819										6.41 × 10 ⁻⁴		
	545.755816										4.35 × 10 ⁻⁴		
	515.170245										9.84 × 10 ⁻³		
	516.922004										1.33 × 10 ⁻³		
	517.676592										4.54 × 10 ⁻⁴		
	521.776019										4.58 × 10 ⁻⁴		
	522.04636										9.08 × 10 ⁻⁴		
	523.306240										5.38 × 10 ⁻⁴		
	524.142239												
	529.038126												
	531.437209												
	531.460073												
	537.151571												
	545.755816												

temperature for CH₃OH can be achieved by fitting the transitions separately based on their upper-state energies. Specifically, transitions with upper state energy below 300 K yield a rotational temperature of 132.41 ± 19.02 K with a column density of (6.18 ± 0.48) × 10¹⁴ cm⁻², while those above 300 K result in a rotational temperature of 227.51 ± 66.76 K with a column density of (1.94 ± 0.35) × 10¹⁵ cm⁻² (see Figure 4).

Applying a similar approach in the MCMC fitting process, we determined an excitation temperature of 117.55 ± 23.58 K for transitions with energy levels below 300 K, corresponding to a column density of (6.24 ± 3.31) × 10¹⁴ cm⁻². For transitions with energy levels above 300 K, the excitation temperature was found to be 240.78 ± 97.12 K, with a column density of (2.80 ± 0.71) × 10¹⁵ cm⁻² (see Table 5). These findings align well with the rotational diagram.

These excitation circumstances are compatible with the hot core environment, where dust temperatures above the sublimation threshold of ice mantles (~100 K) cause thermal desorption of methanol and other molecules into the gas phase (Garrod, 2008). The low optical depths ($\tau < 0.1$) indicate a narrow emission. The extensive excitation conditions indicate that methanol spreads throughout compact, warm, and long moderate-temperature areas, similar to what is reported in other hot cores, such as Orion KL and Sgr B2(N) (Crockett et al., 2014; Tahani et al., 2016).

CARBON MONOXIDE (CO) and its ISOTOPOLOGUES ^{13}CO AND C^{18}O : Carbon monoxide (CO) is the most abundant molecule after H_2 and serves as a key tracer of molecular gas in star-forming regions. Toward G10, we detect the $J = 9-8$ and $J = 10-9$ transitions of CO, with upper-state energies (E_u) of 249 K and 304 K, respectively. The CO line profiles clearly exhibit two distinct components with respect to the systemic velocity (67 km s^{-1}): a narrow blueshifted component and a wing profile in the redshifted zone. We modeled these profiles using a two-component MCMC fit, and the derived parameters are summarized in Table 5. The two-component fit indicates that the narrow, blueshifted component, located 3.5 km s^{-1} from the systemic velocity, has a higher column density but a lower temperature. This component may primarily represent the extended outflow. In contrast, the broad, redshifted component, found at 3 km s^{-1} from the systemic velocity, is characterized by a lower column density and a higher excitation temperature. This component likely corresponds to a minor fraction of the gas heated and kinematically disturbed, possibly due to protostellar activity or outflow-driven shocks near the core.

In addition to the high excitation transition of CO, we also identify high excitation transitions of ^{13}CO as $J = 9-8$ and $J = 11-10$ having $E_u = 237.93 \text{ K}$ and 348.92 K respectively, as well as a transition for C^{18}O ($9-8$) having $E_u = 237.03 \text{ K}$. Unlike carbon monoxide, we only observe a single peak for these isotopologues.

The peaks of ^{13}CO and C^{18}O correspond to the systematic velocity of the source. The measured excitation temperatures are $40.34 \pm 9.16 \text{ K}$ and $64.5 \pm 7.9 \text{ K}$, respectively, which are equal or greater than the blue-shifted narrow component ($41.3 \pm 9.9 \text{ K}$) obtained for CO but lower than the red-shifted component ($104.5 \pm 6.5 \text{ K}$) in Table 5. Therefore, these transitions indicate both the quiescent envelope and the outflow component.

Table 4 shows that the integrated intensity ratio of ^{12}CO to ^{13}CO is 2.7. Similarly, the intensity ratio of ^{12}CO to C^{18}O is 7.5. These ratios are substantially lower than the canonical local-ISM value ($^{12}\text{C}/^{13}\text{C}$ isotopic ratio of 57–74, Langer and Penzias (1993), $^{16}\text{O}/^{18}\text{O}$ ratio of approximately 500, Lodders et al. (2009)). This likely reflects an optical-depth effect, with ^{12}CO appearing optically thick. We have estimated the ^{12}CO line integrated intensity based on that obtained from its rare isotopologues, ^{13}CO (considering $^{12}\text{CO}/^{13}\text{CO} = 65$), which yields a $^{12}\text{CO}/\text{C}^{18}\text{O}$ ratio of 178.

WATER (H_2O): High excitation transitions of ortho-water (o- H_2O) and para-water (p- H_2O) have been detected toward G10 and noted in Table 4. Interestingly, the line profile of p- H_2O exhibits a behavior similar to that of CO. Accordingly, we performed a two-component fit, and the resulting line parameters are listed in Table 5. The narrow blueshifted component (shifted by 3.5 km s^{-1} from the systematic velocity) has an FWHM of $4.5 \pm 0.1 \text{ km s}^{-1}$ for p- H_2O , compared to $5.1 \pm 0.3 \text{ km s}^{-1}$ for CO, with derived excitation temperatures of $30.0 \pm 1.1 \text{ K}$ and $41.3 \pm 9.9 \text{ K}$, respectively. For the broad redshifted component (shifted by 3 km s^{-1} from the systematic velocity), both CO and p- H_2O show a FWHM of $\sim 11 \text{ km s}^{-1}$, with excitation temperatures of $104.5 \pm 6.5 \text{ K}$ for CO and $97.25 \pm 0.1 \text{ K}$ for p- H_2O . We also detected isotopologues of H_2O : H_2^{18}O and H_2^{17}O , with an upper state energy of 100.6 K. The best-fit column densities are noted in Table 5.

HYDROGEN CYANIDE (HCN) and HYDROGEN ISOCYANIDE (HNC): These are well-known indicators of dense molecular gas in star-forming regions (Hacar et al., 2020). Like CO and p- H_2O , the HCN line profile also exhibits a similar pattern, with both blueshifted and redshifted components clearly visible. We fitted the data using two components, and the resulting parameters are presented in Table 5. Similar to the findings for CO and p- H_2O , we observed that the narrow blueshifted component has a higher column density and a lower temperature compared to the redshifted component, which has a lower column density and a higher temperature. Notably, for HCN, the redshifted component is significantly shifted from the systematic velocity by 6.5 km s^{-1} , which is different from the values observed for CO and p- H_2O . This suggests that the emission might originate from dense shocked clumps or the base of an outflow lobe, which is moving at a comparatively faster velocity than the region where CO and p- H_2O emissions were observed. Thus, HCN might trace a localized shocked region, while CO and p- H_2O probably probe the broader warm flow.

However, confirming this requires an imaging analysis of these species, which is beyond the scope of this work. We obtained emission data for HNC, which displays a single peak centered at the systemic velocity. Consequently, we analyzed it using a single component. Interestingly, the single peak arises close to the blueshifted component of the HCN.

CARBON MONOSULFIDE (CS) and its ISOTOPOLOGUE (C^{34}S): The observations of $J = 11 - 10$ transitions of CS and C^{34}S toward G10 provide insights into the dense gas properties of a high-mass star-forming core Plume et al. (1997). Like CO, p- H_2O , and HCN, the profile of the CS line is better represented by a two-component fit shown in Fig. 7 and Table 5. Our

two-component fit shows a similar characteristic: a blueshifted component with a higher column density and lower temperature, in contrast to the redshifted wing, which has a lower column density and a higher temperature. Like HCN, its redshifted wing is more shifted from the systemic velocity than CO and p-H₂O. We detected emission from the isotopologue C³⁴S, which exhibits a single peak at the systemic velocity. A comparison between the total column density derived for CS and that of C³⁴S yields a ratio lower than the canonical elemental ³²S/³⁴S value, indicating that the main CS transition is affected by optical depth and is likely optically thick.

FORMYL CATION (HCO⁺): It is one of the most important tracers of dense molecular gas, as its abundance is sensitive to the ionization fraction, and it is strongly enhanced in shocked or UV-irradiated environments. In G10, the 6 → 5 transition at 535.0614 GHz exhibits a line width of $6.81 \pm 1.14 \text{ km s}^{-1}$, a column density of $(3.75 \pm 1.31) \times 10^{13} \text{ cm}^{-2}$ and an excitation temperature of $23.29 \pm 3.82 \text{ K}$. These results indicate moderate excitation, consistent with conditions in other high-mass star-forming cores, where HCO⁺ effectively traces both quiescent gas and dynamically active regions associated with feedback processes (Gerner et al., 2014).

SULFUR MONOXIDE (SO) and SULFUR DIOXIDE (SO₂): Transitions of SO and SO₂ toward G10, trace regions affected by protostellar feedback and shocks. The SO transitions 12_{1,2} – 11_{1,1} and 12_{1,3} – 11_{1,2} show a broad line width ($6.99 \pm 0.45 \text{ km s}^{-1}$), a moderate excitation temperature ($T_{\text{ex}} = 45.72 \pm 5.55 \text{ K}$) and a column density of $(3.60 \pm 0.98) \times 10^{14} \text{ cm}^{-2}$, all of which indicate a turbulent warm gas. Similar features are displayed by SO₂, which has an excitation temperature of $31.66 \pm 6.70 \text{ K}$ and a column density of $(2.90 \pm 0.87) \times 10^{14} \text{ cm}^{-2}$. According to Bachiller and Pérez Gutiérrez (1997); Esplugues et al. (2014), these sulfur-bearing species are known to act as shock tracers and are frequently amplified in areas where the outflows disturb the surrounding medium, releasing molecules from the mantles of the dust particles. In G10, their presence facilitates dynamic chemical processing and active high-mass star formation.

THIOFORMALDEHYDE (H₂CS): The transitions of H₂CS in G10 exhibit a column density of $(1.65 \pm 0.94) \times 10^{15} \text{ cm}^{-2}$ with an excitation temperature of $54.52 \pm 12.95 \text{ K}$. The moderately broad line widths $8.37 \pm 1.20 \text{ km s}^{-1}$ shown in Table 5 and the extended emission suggest its association with warm, dense, and possibly shocked gas. A valuable indicator of early-stage sulfur chemistry in hot cores, H₂CS is known to arise by gas-phase and grain-surface processes (Hatchell et al., 1998; van der Tak et al., 2003). Its existence confirms the high temperatures and vigorous chemical evolution in high-mass star-forming regions.

AMINO RADICAL (NH₂): The hyperfine transitions of the amino radical at 993.322971 GHz ($E_u = 167.8 \text{ K}$) are observed toward G10. We obtain a good fit to the observed spectra with a column density of $(3.6 \pm 0.6) \times 10^{14} \text{ cm}^{-2}$ and an excitation temperature of 31 K.

Here, CO, p-H₂O, HCN, and CS exhibit a similar profile. The last column of Table 5 shows the optical depth for each transition under the LTE approximation, indicating that all considered transitions are optically thin. To further verify this, we conducted a separate analysis using the RADEX code, a non-LTE radiative transfer tool for modeling molecular line emissions (van der Tak et al., 2007). For our analysis, we adopted a hydrogen number density of $8.52 \times 10^5 \text{ cm}^{-3}$, derived from the parameters fitted to our spectral energy distribution (SED) (see Section 3.1). Additionally, we assumed the excitation temperature, full width at half maximum (FWHM), and column density values listed in Table 5. For each species with available collisional rates, we utilized data from the LAMDA database (Schöier et al., 2005), except for C³⁴S. For H₂CS, collisional rates for the observed transitions were not available. Under these conditions, we confirmed that all transitions investigated were optically thin. Also in Table 6, estimated abundances of the species were derived from the column density obtained through the MCMC fitting.

In addition to the detected emission lines, we identify two transitions of OH⁺ and two transitions of NH in absorption, along with one absorption transition of H₂S and one transition of ammonia. Previous observations by van Dishoeck et al. (2021) have reported OH⁺ in absorption toward G10.47+0.03. A detailed radiative transfer and chemical modeling of these absorption features is beyond the scope of the present work and will be presented in a forthcoming study.

3.3 New Insights from the Herschel High-Frequency Observations

Earlier observations establish G10 as a chemically rich, compact hot molecular core embedded in a massive clump and closely associated with ultracompact H II regions (Cesaroni et al., 2010; Rolffs et al., 2011; Gorai et al., 2020a; Mondal et al., 2021, 2023), but a uniform far-IR/submm line census or a detailed excitation and kinematic decomposition across many key tracers

Table 6. Estimated abundances were derived from the column density obtained through the MCMC fitting presented in Table 5. For this estimation, we consider $N_{\text{H}_2} = 6.74 \times 10^{23} \text{ cm}^{-2}$, as indicated in Section 3.1.

Species	Column Density (cm^{-2})	Fractional Abundance
SO	$(3.60 \pm 0.98) \times 10^{14}$	$(5.34 \pm 3.94) \times 10^{-10}$
SO ₂	$(2.90 \pm 0.87) \times 10^{14}$	$(4.30 \pm 3.33) \times 10^{-10}$
CS	$(7.85 \pm 5.4) \times 10^{13}$ $(4.31 \pm 1.29) \times 10^{13}$	$(1.16 \pm 1.37) \times 10^{-10}$ $(0.64 \pm 0.49) \times 10^{-10}$
C ³⁴ S	$(2.91 \pm 0.52) \times 10^{13}$	$(0.43 \pm 0.26) \times 10^{-10}$
H ₂ ¹⁸ O	$(1.37 \pm 0.5) \times 10^{14}$	$(2.03 \pm 1.74) \times 10^{-10}$
H ₂ ¹⁷ O	$(8.40 \pm 4.20) \times 10^{13}$	$(1.25 \pm 1.24) \times 10^{-10}$
o-H ₂ O	$(1.69 \pm 0.43) \times 10^{16}$	$(2.51 \pm 1.79) \times 10^{-8}$
p-H ₂ O	$(6.33 \pm 0.4) \times 10^{13}$ $(4.81 \pm 0.4) \times 10^{13}$	$(0.94 \pm 0.33) \times 10^{-10}$ $(0.71 \pm 0.29) \times 10^{-10}$
HCN	$(1.10 \pm 0.90) \times 10^{14}$ $(1.72 \pm 0.60) \times 10^{13}$	$(1.63 \pm 2.09) \times 10^{-10}$ $(2.55 \pm 2.13) \times 10^{-11}$
HNC	$(2.86 \pm 0.70) \times 10^{13}$	$(4.24 \pm 2.96) \times 10^{-11}$
NH ₂	$(3.60 \pm 0.60) \times 10^{13}$	$(5.34 \pm 3.08) \times 10^{-11}$
HCO ⁺	$(3.75 \pm 1.31) \times 10^{13}$	$(5.56 \pm 4.65) \times 10^{-11}$
C ¹⁸ O	$(1.8 \pm 0.53) \times 10^{16}$	$(2.67 \pm 2.05) \times 10^{-8}$
¹³ CO	$(1.80 \pm 0.85) \times 10^{17}$	$(2.67 \pm 2.59) \times 10^{-7}$
CO	$(5.5 \pm 2.3) \times 10^{16}$ $(3.7 \pm 0.6) \times 10^{16}$	$(8.16 \pm 7.46) \times 10^{-8}$ $(5.49 \pm 3.13) \times 10^{-8}$
H ₂ CS	$(1.65 \pm 0.94) \times 10^{15}$	$(2.44 \pm 2.61) \times 10^{-9}$
CH ₃ OH (E _u < 300 K)	$(6.24 \pm 3.31) \times 10^{14}$	$(9.26 \pm 9.53) \times 10^{-10}$
CH ₃ OH (E _u > 300 K)	$(2.80 \pm 0.71) \times 10^{15}$	$(4.15 \pm 2.96) \times 10^{-9}$

has not been reported. Against this backdrop, the new contribution of the present *HIFI* archival data analysis is a homogeneous far-IR spectral view of this source. This study expands the inventory of detected species to include multiple isotopologues and high-excitation (>100 K) transitions of CO, HCN, ¹³CO, C¹⁸O, CS, C³⁴S, SO, ortho-/para-H₂O, H₂¹⁸O, H₂CS, and CH₃OH. In particular, the detection of a high-excitation CO transition in this source is new and directly probes warmer and denser gas than the low-*J* CO transitions commonly targeted in earlier work, extending the diagnostic reach of CO to the hot inner regions sampled by *HIFI*. The CH₃OH rotational-diagram analysis reveals two temperature components (~132 K from low-*E*_{up} lines and ~228 K from high-*E*_{up} lines), supported by MCMC fitting. This result places the methanol-emitting gas into at least two physically distinct temperature regimes, refining earlier single-temperature characterizations often assumed when only limited transitions spanning a narrow range of *E*_{up} were available. Moreover, the simultaneous detection of grain-surface products (CH₃OH and ortho-/para-H₂O, including H₂¹⁸O) together with multiple sulfur-bearing species (SO, SO₂, and CS isotopologues) provides a chemically consistent picture in which shocks or outflow activity desorb ice mantles and rapidly drive sulfur chemistry, thereby linking the chemistry more directly. Finally, by fitting line profiles of CO, para-H₂O, HCN, and CS with distinct narrow and broad components, the analysis separates cooler, narrow outflow-layer gas from warmer, dynamically active gas likely associated with inner outflows or shocks. This complements the prior view of G10 as a compact, active hot core by adding a quantitative, multi-tracer kinematic decomposition in the far-IR. Furthermore, various protostellar properties have been derived through spectral energy distribution (SED) analysis using archival *Spitzer*/IRAC (3.6–8.0 μm), MIPS 24 μm , and *Herschel*/PACS–SPIRE (70–500 μm) data. This analysis also provides estimates of column densities, which are subsequently used to determine the fractional abundances of all detected species.

4 CONCLUSIONS

In this work, we present a spectral survey of G10 using Herschel archival data covering the frequency range 515–1226 GHz. We provide a detailed analysis of its molecular line inventory, which reveals a chemically rich and dynamically complex environment

typical of high-mass star-forming regions. This study represents the first investigation of the spectral properties of this source over this frequency range. The main conclusions are as follows.

- We detected a wide range of molecular species shown in Table 3, including CO, HCN, HCO^+ , ^{13}CO , C^{18}O , HNC, CS, C^{34}S , SO, SO_2 , o- H_2O , p- H_2O , H_2^{18}O , H_2CS , and CH_3OH . Multiple transitions of CH_3OH and H_2CS were identified. This is the first time that a high excitation transition of carbon monoxide (CO) has been identified in this source.
- The rotational diagram of CH_3OH in Figure 4 reveals two temperature components. The first component, with $T = 132.41 \pm 19.02$ K is derived from low-excitation transitions ($E_{\text{up}} < 300$ K) of CH_3OH . The second, warmer component, with $T = 227.51 \pm 66.76$ K, is obtained from the high-excitation transitions ($E_{\text{up}} > 300$ K) of CH_3OH . Our MCMC results in Table 5 further support this. Our measured temperatures from MCMC fitting are consistent with those obtained using the rotational diagram analysis.
- We detect sulfur-bearing species, methanol, and water in both ortho and para forms. Methanol and water are known to form predominantly on dust-grain ice mantles. The coexistence of these species with sulfur-bearing molecules—commonly enhanced in shocked environments—strongly suggests shock-induced desorption of ice mantles followed by rapid gas-phase chemical processing. Isotopologue detections across multiple excitation conditions further constrain the thermal structure of the core and its density distribution.
- Our best-fit SED modeling constrains the key physical parameters of G10, including the visual extinction, the total mass of the dense molecular core surrounding the protostar, the mass of the central protostar, the mass surface density of the core, the envelope mass, the core radius, and the bolometric luminosity estimated both under the assumption of isotropic emission and as an average over different inclination angles. These constraints provide crucial insight into the evolutionary stage of G10, helping to refine our understanding of the physical processes driving massive star formation in this region. They also serve as a benchmark for future molecular line studies and detailed chemo-dynamical modeling.
- The line profiles obtained for CO, p- H_2O , HCN, and CS exhibit similarities. The MCMC fitting indicates that the narrow components likely trace the outer layer of the outflow. This is indicated by their obtained best fit with small velocity widths ($\sim 5 \text{ km s}^{-1}$) and blue-shifted peaks (shifted by $\sim 3.5 \text{ km s}^{-1}$) relative to the systemic velocity, along with a temperature range of 24 K to 41 K. In contrast, the broad red-shifted (shifted by $\sim 3 \text{ km s}^{-1}$) for CO and p- H_2O and by $6.5\text{--}6.8 \text{ km s}^{-1}$ for HCN and CS probably originates from dynamically active gas associated with the inner layers of the outflows or shocks, which has a temperature of approximately 100 K. While the line survey provides detailed chemical and kinematic information, complementary imaging observations would offer spatial context and reveal the distribution of these species across the source.

DATA AVAILABILITY STATEMENT

The original contributions presented in the study are included in the article/Supplementary Material; further inquiries can be directed to the corresponding author.

CONFLICT OF INTEREST STATEMENT

The authors declare that the research was conducted in the absence of any commercial or financial relationships that could be construed as a potential conflict of interest.

AUTHOR CONTRIBUTIONS

All authors listed have made a substantial, direct, and intellectual contribution to the work and approved it for publication.

ACKNOWLEDGMENT

R.F. acknowledges support from the grants PID2023-146295NB-I00, and from the Severo Ochoa grant CEX2021-001131-S funded by MCIN/AEI/ 10.13039/501100011033 and by “European Union NextGenerationEU/PRTR”.

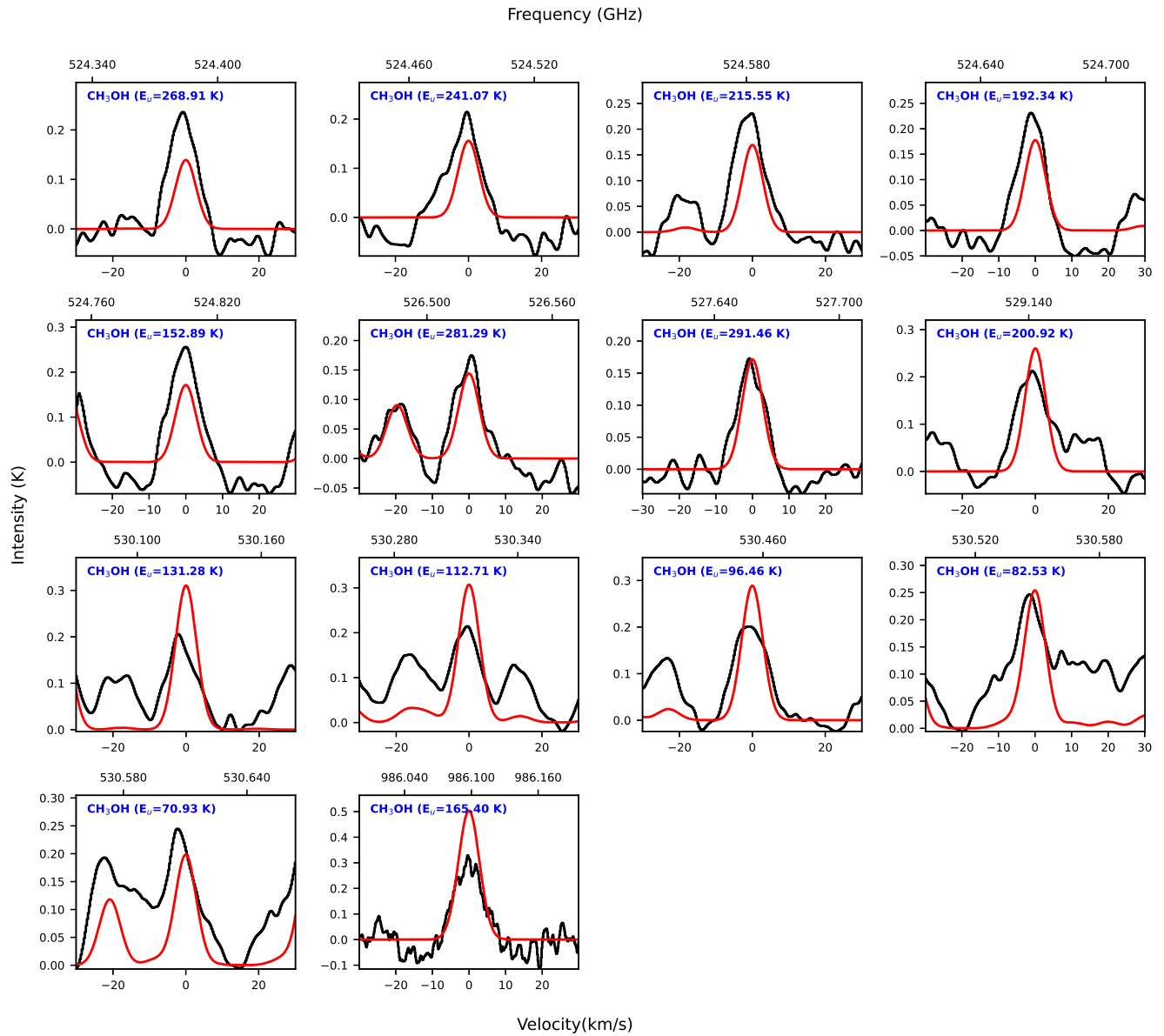


Figure 5. MCMC fitting of observed lines of CH_3OH ($vt=0-2$) below 300 K toward G10. Black lines represent the observed spectra and red lines the synthetic spectra.

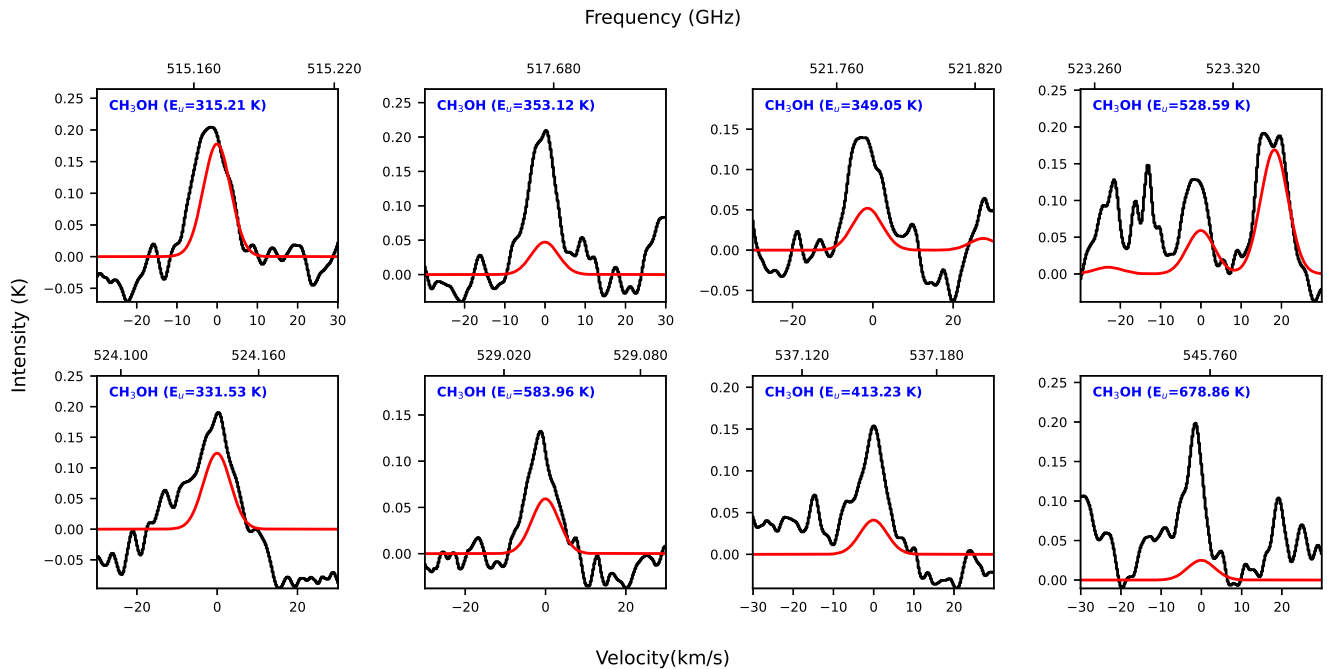


Figure 6. MCMC fitting of observed lines of CH_3OH ($vt=0-2$) above 300 K toward G10. Black lines represent the observed spectra and red lines the synthetic spectra.

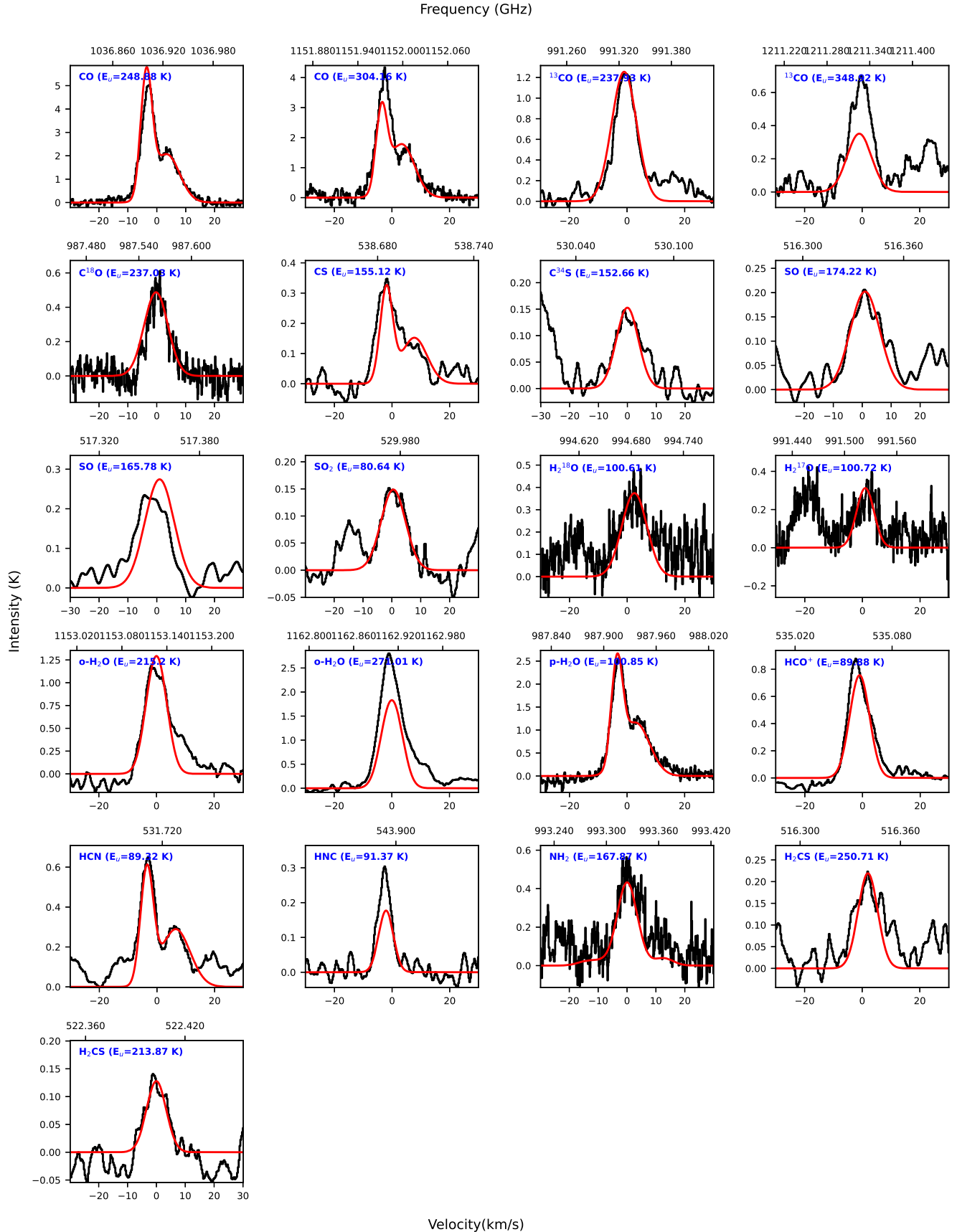


Figure 7. MCMC fitting of observed lines of CO and its isotopologues, CS, C^{34}S , SO, SO_2 , H_2O , HCO^+ , HCN, HNC, NH_2 , and H_2CS toward G10. Black lines represent the observed spectra and red lines the synthetic spectra.

REFERENCES

Bachiller, R. and Pérez Gutiérrez, M. (1997). Shock Chemistry in the Young Bipolar Outflow L1157. *apjl* 487, L93–L96. doi: 10.1086/310877

Belloche, A., Garrod, R. T., Müller, H. S. P., Menten, K. M., Comito, C., and Schilke, P. (2009). Increased complexity in interstellar chemistry: detection and chemical modeling of ethyl formate and n-propyl cyanide in Sagittarius B2(N). *aap* 499, 215–232. doi: 10.1051/0004-6361/200811550

Belloche, A., Garrod, R. T., Müller, H. S. P., Menten, K. M., Medvedev, I., Thomas, J., et al. (2019). Re-exploring Molecular Complexity with ALMA (ReMoCA): interstellar detection of urea. *aap* 628, A10. doi: 10.1051/0004-6361/201935428

Bergin, E. A., Phillips, T. G., Comito, C., Crockett, N. R., Lis, D. C., Schilke, P., et al. (2010). Herschel observations of EXtra-Ordinary Sources (HEXOS): The present and future of spectral surveys with Herschel/HIFI. *aap* 521, L20. doi: 10.1051/0004-6361/201015071

[Dataset] Bradley, L., Sipőcz, B., Robitaille, T., Tollerud, E., Vinícius, Z., Deil, C., et al. (2020). Astropy photutils: Version 1.0.0. doi: 10.5281/zenodo.4044744. Zenodo software release

Ceccarelli, C., Bacmann, A., Boogert, A., Caux, E., Dominik, C., Lefloch, B., et al. (2010). Herschel spectral surveys of star-forming regions. Overview of the 555–636 GHz range. *aap* 521, L22. doi: 10.1051/0004-6361/201015081

Cesaroni, R., Hofner, P., Araya, E., and Kurtz, S. (2010). The structure of hot molecular cores over 1000 AU. *aap* 509, A50. doi: 10.1051/0004-6361/200912877

Crockett, N. R., Bergin, E. A., Neill, J. L., Favre, C., Schilke, P., Lis, D. C., et al. (2014). Herschel observations of extraordinary sources: Analysis of the hifi 1.2 thz wide spectral survey toward orion kl. i. methods. *The Astrophysical Journal* 787, 112. doi: 10.1088/0004-637x/787/2/112

Das, A. (2024). Astrochemistry: The study of chemical processes in space. *Life Sciences in Space Research* 43, 43–53. doi: <https://doi.org/10.1016/j.lssr.2024.10.005>. Life Sciences in Space Research Tenth Anniversary Special Issue

de Graauw, T., Helmich, F. P., Phillips, T. G., Stutzki, J., Caux, E., Whyborn, N. D., et al. (2010). The Herschel-Heterodyne Instrument for the Far-Infrared (HIFI). *aap* 518, L6. doi: 10.1051/0004-6361/201014698

De Luca, M., Gupta, H., Neufeld, D., Gerin, M., Teyssier, D., Drouin, B. J., et al. (2012). Herschel/HIFI Discovery of HCl⁺ in the Interstellar Medium. *apjl* 751, L37. doi: 10.1088/2041-8205/751/2/L37

Esplugues, G. B., Viti, S., Goicoechea, J. R., and Cernicharo, J. (2014). Modelling the sulphur chemistry evolution in Orion KL. *aap* 567, A95. doi: 10.1051/0004-6361/201323010

Fazio, G. G., Hora, J. L., Allen, L. E., Ashby, M. L. N., Barmby, P., Deutsch, L. K., et al. (2004). The Infrared Array Camera (IRAC) for the Spitzer Space Telescope. *apjs* 154, 10–17. doi: 10.1086/422843

Fedriani, R., Tan, J. C., Telkamp, Z., Zhang, Y., Yang, Y.-L., Liu, M., et al. (2023). The SOFIA Massive (SOMA) Star Formation Survey. IV. Isolated Protostars. *apj* 942, 7. doi: 10.3847/1538-4357/aca4cf

Garrod, R. T. (2008). A new modified-rate approach for gas-grain chemical simulations. *aap* 491, 239–251. doi: 10.1051/0004-6361:200810518

Garrod, R. T. (2013). A Three-phase Chemical Model of Hot Cores: The Formation of Glycine. *apj* 765, 60. doi: 10.1088/0004-637X/765/1/60

Gerner, T., Beuther, H., Semenov, D., Linz, H., Vasyunina, T., Bihl, S., et al. (2014). Chemical evolution in the early phases of massive star formation. i. *A and A* 563, A97. doi: 10.1051/0004-6361/201322541

Goldsmith, P. F. and Langer, W. D. (1999). Population Diagram Analysis of Molecular Line Emission. *apj* 517, 209–225. doi: 10.1086/307195

Gorai, P., Bhat, B., Sil, M., Mondal, S. K., Ghosh, R., Chakrabarti, S. K., et al. (2020a). Identification of Prebiotic Molecules Containing Peptide-like Bonds in a Hot Molecular Core, G10.47+0.03. *apj* 895, 86. doi: 10.3847/1538-4357/ab8871

Gorai, P., Bhat, B., Sil, M., Mondal, S. K., Ghosh, R., Chakrabarti, S. K., et al. (2020b). Identification of Prebiotic Molecules Containing Peptide-like Bonds in a Hot Molecular Core, G10.47+0.03. *apj* 895, 86. doi: 10.3847/1538-4357/ab8871

Griffin, M. J., Abergel, A., Abreu, A., Ade, P. A. R., André, P., Augueres, J.-L., et al. (2010). The Herschel-SPIRE instrument and its in-flight performance. *aap* 518, L3. doi: 10.1051/0004-6361/201014519

Hacar, A., Bosman, A. D., and van Dishoeck, E. F. (2020). HCN-to-HNC intensity ratio: a new chemical thermometer for the molecular ISM. *aap* 635, A4. doi: 10.1051/0004-6361/201936516

Hatchell, J., Thompson, M. A., Millar, T. J., and MacDonald, G. H. (1998). Sulphur chemistry and evolution in hot cores. *aap* 338, 713–722

Jørgensen, J. K., Belloche, A., and Garrod, R. T. (2020). Astrochemistry During the Formation of Stars. *ARA&A* 58, 727–778. doi: 10.1146/annurev-astro-032620-021927

Kama, M., López-Sepulcre, A., Dominik, C., Ceccarelli, C., Fuente, A., Caux, E., et al. (2013). The Herschel/HIFI spectral survey of OMC-2 FIR 4 (CHESS). An overview of the 480 to 1902 GHz range. *aap* 556, A57. doi: 10.1051/0004-6361/201219431

Kazmierczak, M., Tak, F., Helmich, F., Chavarría, L., Wang, K., and Ceccarelli, C. (2014). The hifi spectral survey of afgl 2591 (chess). ii. summary of the survey. *Astronomy and Astrophysics* 567. doi: 10.1051/0004-6361/201322819

Langer, W. D. and Penzias, A. A. (1993). 12C/ 13C Isotope Ratio in the Local Interstellar Medium from Observations of 13C 18O in Molecular Clouds. *apj* 408, 539. doi: 10.1086/172611

Ligterink, N., Walsh, C., Cuppen, H., Drozdovskaya, M., Ahmad, A., Benoit, D., et al. (2025). Molecular mobility of extraterrestrial ices: surface diffusion in astrochemistry and planetary science. *Physical Chemistry Chemical Physics* 27, 19630–19641

Lodders, K., Palme, H., and Gail, H. (2009). 4.4 abundances of the elements in the solar system. *Solar system*, 712–770

McGuire, B. A. (2022). 2021 Census of Interstellar, Circumstellar, Extragalactic, Protoplanetary Disk, and Exoplanetary Molecules. *apjs* 259, 30. doi: 10.3847/1538-4365/ac2a48

Menten, K. M., Reid, M. J., Forbrich, J., and Brunthaler, A. (2007). The distance to the orion nebula. *Aand A* 474, 515–520. doi: 10.1051/0004-6361:20078247

Mondal, S. K., Chakrabarti, S. K., Das, A., and Gorai, P. (2021). A combined observational and theoretical study to understand the evolution of nitrogen-bearing species in high-mass star-forming regions. In *43rd COSPAR Scientific Assembly. Held 28 January - 4 February*. vol. 43, 1924

Mondal, S. K., Iqbal, W., Gorai, P., Bhat, B., Wakelam, V., and Das, A. (2023). Investigating the hot molecular core, G10.47+0.03: A pit of nitrogen-bearing complex organic molecules. *aap* 669, A71. doi: 10.1051/0004-6361/202243802

Müller, H. S. P., Schlöder, F., Stutzki, J., and Winnewisser, G. (2005). The Cologne Database for Molecular Spectroscopy, CDMS: a useful tool for astronomers and spectroscopists. *Journal of Molecular Structure* 742, 215–227. doi: 10.1016/j.molstruc.2005.01.027

Müller, H. S. P., Thorwirth, S., Roth, D. A., and Winnewisser, G. (2001). The Cologne Database for Molecular Spectroscopy, CDMS. *aap* 370, L49–L52. doi: 10.1051/0004-6361:20010367

Nagy, Z., Choi, Y., Ossenkopf-Okada, V., van der Tak, F. F. S., Bergin, E. A., Gerin, M., et al. (2017). Herschel/hifi spectral line survey of the orion bar: Temperature and density differentiation near the pdr surface. *Aand A* 599, A22. doi: 10.1051/0004-6361/201628916

Pickett, H. M., Poynter, R. L., Cohen, E. A., Delitsky, M. L., Pearson, J. C., and Müller, H. S. P. (1998). Submillimeter, millimeter and microwave spectral line catalog. *jqsrt* 60, 883–890. doi: 10.1016/S0022-4073(98)00091-0

Pilbratt, G. L., Riedinger, J. R., Passvogel, T., Crone, G., Doyle, D., Gageur, U., et al. (2010). Herschel Space Observatory. An ESA facility for far-infrared and submillimetre astronomy. *aap* 518, L1. doi: 10.1051/0004-6361/201014759

Plume, R., Jaffe, D. T., Evans, I., Neal J., Martín-Pintado, J., and Gómez-González, J. (1997). Dense Gas and Star Formation: Characteristics of Cloud Cores Associated with Water Masers. *apj* 476, 730–749. doi: 10.1086/303654

Rivilla, V. M., Jiménez-Serra, I., Martín-Pintado, J., Briones, C., Rodríguez-Almeida, L. F., Rico-Villas, F., et al. (2021). Discovery in space of ethanolamine, the simplest phospholipid head group. *Proceedings of the National Academy of Science* 118, e2101314118. doi: 10.1073/pnas.2101314118

Roelfsema, P. R., Helmich, F. P., Teyssier, D., Ossenkopf, V., Morris, P., Olberg, M., et al. (2012). In-orbit performance of Herschel-HIFI. *aap* 537, A17. doi: 10.1051/0004-6361/201015120

Rolffs, R., Schilke, P., Zhang, Q., and Zapata, L. (2011). Structure of the hot molecular core G10.47+0.03. *aap* 536, A33. doi: 10.1051/0004-6361/201117112

Schöier, F. L., van der Tak, F. F. S., van Dishoeck, E. F., and Black, J. H. (2005). An atomic and molecular database for analysis of submillimetre line observations. *aap* 432, 369–379. doi: 10.1051/0004-6361:20041729

Tahani, K., Plume, R., Bergin, E. A., Tolls, V., Phillips, T. G., Caux, E., et al. (2016). Analysis of the herschel/hexos spectral survey toward orion south: A massive protostellar envelope with strong external irradiation. *The Astrophysical Journal* 832, 12. doi: 10.3847/0004-637x/832/1/12

Telkamp, Z., Fedriani, R., Tan, J. C., Law, C.-Y., Zhang, Y., Plunkett, A., et al. (2025). The SOFIA Massive (SOMA) Star Formation Survey. V. Clustered Protostars. *apj* 986, 15. doi: 10.3847/1538-4357/adcd79

Urquhart, J. S., König, C., Giannetti, A., Leurini, S., Moore, T. J. T., Eden, D. J., et al. (2018). ATLASGAL - properties of a complete sample of Galactic clumps. *MNRAS* 473, 1059–1102. doi: 10.1093/mnras/stx2258

van der Tak, F. F. S., Black, J. H., Schöier, F. L., Jansen, D. J., and van Dishoeck, E. F. (2007). A computer program for fast non-lte analysis of interstellar line spectra. *Astronomy and Astrophysics* 468, 627–635. doi: 10.1051/0004-6361:20066820

van der Tak, F. F. S., Boonman, A. M. S., Braakman, R., and van Dishoeck, E. F. (2003). Sulphur chemistry in the envelopes of massive young stars. *aap* 412, 133–145. doi: 10.1051/0004-6361:20031409

van der Tak, F. F. S., Chavarria, L., Herpin, F., Wyrowski, F., Walmsley, C. M., van Dishoeck, E. F., et al. (2013a). Water in star-forming regions with Herschel (WISH). IV. A survey of low-J H₂O line profiles toward high-mass protostars. *aap* 554, A83. doi: 10.1051/0004-6361/201220976

van der Tak, F. F. S., Chavarria, L., Herpin, F., Wyrowski, F., Walmsley, C. M., van Dishoeck, E. F., et al. (2013b). Water in star-forming regions with Herschel (WISH). IV. A survey of low-J H₂O line profiles toward high-mass protostars. *aap* 554, A83. doi: 10.1051/0004-6361/201220976

van Dishoeck, E. F. and Blake, G. A. (1998). Chemical Evolution of Star-Forming Regions. *ARA&A* 36, 317–368. doi: 10.1146/annurev.astro.36.1.317

van Dishoeck, E. F., Kristensen, L. E., Mottram, J. C., Benz, A. O., Bergin, E. A., Caselli, P., et al. (2021). Water in star-forming regions: physics and chemistry from clouds to disks as probed by Herschel spectroscopy. *aap* 648, A24. doi: 10.1051/0004-6361/202039084

Vastel, C., Bottinelli, S., Caux, E., Glorian, J. M., and Boizot, M. (2015). CASSIS: a tool to visualize and analyse instrumental and synthetic spectra. In *SF2A-2015: Proceedings of the Annual meeting of the French Society of Astronomy and Astrophysics*. 313–316

Werner, M. W., Roellig, T. L., Low, F. J., Rieke, G. H., Rieke, M., Hoffmann, W. F., et al. (2004). The Spitzer Space Telescope Mission. *apjs* 154, 1–9. doi: 10.1086/422992

Zernickel, A., Schilke, P., Schmiedeke, A., Lis, D., Brogan, C., Ceccarelli, C., et al. (2012). Molecular line survey of the high-mass star-forming region ngc 6334i with herschel/hifi and the sma. *Astronomy and Astrophysics* 546. doi: 10.1051/0004-6361/201219803

Zhang, Y. and Tan, J. C. (2018). Radiation Transfer of Models of Massive Star Formation. IV. The Model Grid and Spectral Energy Distribution Fitting. *apj* 853, 18. doi: 10.3847/1538-4357/aaa24a